RESEARCH ARTICLE | SEPTEMBER 01 2023

Near-wake structures of a finite square cylinder with a flapping film at its free end

Chongyu Zhao (赵崇宇) ; Hanfeng Wang (王汉封) ; Zhiwei Liu (刘治威) ; Md. Mahbub Alam ;
Hui Tang (唐辉)

Physics of Fluids 35, 095102 (2023)
https://doi.org/10.1063/5.0153537

Physics of Fluids ARTICLE pubs.aip.org/aip/pof

Near-wake structures of a finite square cylinder with a flapping film at its free end

Cite as: Phys. Fluids **35**, 095102 (2023); doi: 10.1063/5.0153537
Submitted: 9 April 2023 · Accepted: 14 August 2023 ·
Published Online: 1 September 2023

View Online Export Citation CrossMark

Chongyu Zhao (赵崇宇),[1,2] Hanfeng Wang (王汉封),[1,3,a)] Zhiwei Liu (刘治威),[1] Md. Mahbub Alam,[4] and Hui Tang (唐辉)[5]

AFFILIATIONS

[1]School of Civil Engineering, Central South University, Changsha, Hunan 410075, China
[2]Department of Earth and Environmental Sciences, The University of Manchester, Manchester M13 9PL, United Kingdom
[3]National Research center for High-speed Railway construction, Changsha, Hunan 410075, China
[4]Center for Turbulence Control, Harbin Institute of Technology (Shenzhen), Shenzhen, Guangdong 518055, China
[5]Research Center for Fluid-Structure Interactions, Department of Mechanical Engineering, The Hong Kong Polytechnic University, Kowloon, Hong Kong 999077, China

[a)]Author to whom correspondence should be addressed: wanghf@csu.edu.cn

ABSTRACT

As a follow-up study of Wang *et al.* ["Control of the flow around a finite square cylinder with a flexible plate attached at the free end," Phys. Fluids **34**(2), 027109 (2022)], this paper presents an experimental study of flow around a wall-mounted finite square cylinder with a vertically clamped flapping film at its free end. The width (d) of the square cylinder was 40 mm, and the aspect ratio (H/d) was 5, where the height H was 200 mm. The flexible film was made of low-density polyethylene, with a thickness of 0.04 mm and the width and length (l) each of d. Flow visualization and particle image velocimetry were conducted in the central lateral plane and several horizontal planes to reveal the 3D structure of the flapping induced vortex (FIV) and its effects on the cylinder near wake. All measurements were done in a low-speed wind tunnel at a flow speed of $U_\infty = 5$ m/s with a Reynolds number of 13 700 based on U_∞ and d. Previous study suggests that the flapping film reduces aerodynamic forces of the cylinder significantly and that the fluctuating lateral force is reduced by 60% [Wang *et al.*, "Control of the flow around a finite square cylinder with a flexible plate attached at the free end," Phys. Fluids **34**(2), 027109 (2022)]. Vortices that shed from the trailing edge of the flapping film connect those from the side edges, forming n-shape FIVs downstream. FIVs induce more high-speed flow downwards into the wake, which suppresses the mean recirculation zone near the free end but enlarges it in the lower part of the wake. The two legs of n-shape FIVs are symmetrically arranged near the cylinder free end, whose effects diminish gradually as approaching the bottom wall, where alternating Karman vortex shedding still prevails.

I. INTRODUCTION

With typical applications in engineering like wind loads on high-rise buildings and structures, aerodynamic characteristics and near-wake structures of a finite square cylinder have long been a field of intensive research over the past few decades (Kikuchi *et al.*, 1997; Kim *et al.*, 2015; Maruta *et al.*, 1998; Menicovich *et al.*, 2014; Mooneghi and Kargarmoakhar, 2016; Zheng and Zhang, 2012; Rastan *et al.* 2017; and Mashhadi *et al.* 2021). Flow around a finite square cylinder is much more complex compared with its 2D counterparts because of the effects of the free end, cylinder-wall junction, finite span, etc. (Rastan *et al.*, 2021; Saeedi *et al.*, 2014; Sumner *et al.*, 2017; Sohankar *et al.* 2018; Wang and Zhou, 2009; and Wang *et al.*, 2006). The typical near wake of a finite cylinder contains free-end downwash flow, spanwise shear flow, and possible upwash flow from the bottom (Bourgeois *et al.*, 2011, 2012; McClean and Sumner, 2014; and Wang and Zhou, 2009). Wang and Zhou (2009), suggesting that the downwash flow induced by the tip vortex connects the spanwise shear flows from both sides of the finite cylinder, forming an "arch-type vortex" structure in the near wake. Furthermore, there are two typical patterns of this arch-type vortex, i.e., anti-symmetrical (Regime A) and symmetrical (Regime B) spanwise vortex shedding. The occurrence probabilities of these two typical patterns are closely related to the aerodynamic performance of the finite cylinder. The anti-symmetrical vortex shedding (Regime A) results in a higher mean drag and fluctuating lateral force on the cylinder than the symmetrical vortex shedding (Regime B). In addition, a low-frequency signature in the flow near the cylinder free end was reported by Kindree *et al.*, (2018) and Peng *et al.*, (2019), which associates with the shift between the two typical vortex shedding modes. This low-frequency behavior is connected with the up-down flapping of the free-end shear flow, which is about 1/10 of the spanwise Karman vortex shedding frequency (Peng *et al.*, 2019).

Inspired by the potential impact of the free-end shear flow on the overall near-wake structure, some passive and active flow control strategies were proposed to optimize the aerodynamic performance of finite cylinders (e.g., Park and Lee 2004; Rinoshika *et al.* 2017; Sohankar *et al.* 2019; Rastan *et al.* 2019; and Wang *et al.* 2020). Park and Lee (2004) studied the influence of free-end configuration on the flow around a finite circular cylinder with an aspect ratio $H/d = 6$. They suggested that the width of the recirculation region and the separation bubble was largely reduced by chamfering and rounding the edges of the free end. An inclined hole connecting the free end and the leeward surface was proposed by Rinoshika *et al.* (2017) to control the flow around a finite circular cylinder of $H/d = 1$. They found a shrunk rear recirculation zone and contracted the separation region on the free end. As for active control strategies, a steady slot suction at the free-end leading edge can suppress the fluctuating lateral force and vortex-induced vibration of a finite square cylinder with $H/d = 5$, as reported by Li *et al.* (2019) and Wang *et al.* (2018). Similarly, a dual-synthetic jet at the free-end leading edge was also proved valid for modulating the flow around a finite square cylinder with $H/d = 4$ (Li *et al.* 2021), with the maximum reduction in the fluctuating lateral force of about 30%. These previous investigations confirmed that a reasonable local perturbation at the free end may lead to a remarkable modulation of the entire flow around the finite cylinder, improving its aerodynamic performance effectively.

A flexible film flapping periodically with large amplitude under specific flow conditions results in large-scale vortices downstream, which was widely used to realize flow control and energy harvesting (Jin *et al.*, 2018a, 2018b; Joshi *et al.*, 2015; Chen *et al.*, 2020; Kumar *et al.*, 2021; Shivashankar and Gopalakrishnan, 2020; Cui and Feng, 2022; Shao *et al.*, 2023; and Zhang *et al.*, 2023). Lee *et al.*, (2017, 2018), Singh and Lakkaraju (2019), Amini and Habibi (2022), and Xu *et al.* (2019) utilized flexible films to improve the heat exchange in the channel flow and enhance the mixing at a jet nozzle exit. Inspired by the landing approach of birds, Brücker and Weidner (2014) and Fang *et al.* (2019) introduced film arrays on the upper surface of an airfoil to delay its stall. The major difference between film-covered and clean airfoils is the flow evolution along the upper surfaces. Regular vortices induced by the flapping film dominate the former, while irregular flow separation leading to a rapid non-linear transition into stall prevails for the latter (Brücker and Weidner, 2014). In addition, extensive efforts have been made to understand the effects of a flexible film attached to the rear of a bluff body on its aerodynamic performance (Liang *et al.*, 2018; Niu and Hu, 2011; Sharma and Dutta, 2020; Wu *et al.*, 2014a, 2014b; Kim and Alam, 2015; Ameya *et al.*, 2020; Cui *et al.*, 2022; Mao *et al.*, 2022, 2023; and Shao *et al.*, 2023). The fluctuating lateral force and the associated fluid-induced vibration can be remarkably attenuated, together with the suppression of spanwise vortex shedding.

Recently, Wang *et al.*, (2022) employed a flexible film at the free-end leading edge to control the aerodynamic forces of a finite square cylinder with $H/d = 5$. They noticed that, once the oncoming flow velocity U_∞ exceeds a critical velocity U_c, the flexible film flaps periodically with the flapping frequency increasing almost linearly with U_∞. The coefficients of aerodynamic forces, i.e., time-averaged drag coefficient (C_d), fluctuating drag coefficient (C_d'), and fluctuating lateral force coefficient (C_l'), reduce by about 5%, 25%, and 60%, respectively, under the influence of the flapping film. Moreover, this reduction is insensitive to the flapping frequency of the film. They also suggested that the flapping-induced vortices (FIVs) in the free-end shear layer enhance the momentum transport between the free stream and the near wake, thus suppressing the spanwise vortex shedding and associated aerodynamic forces. However, the details of the modulation on the near-wake structures by the flapping film have not been thoroughly revealed yet.

The present paper reports an experimental study on the near-wake structure of a finite square cylinder of $H/d = 5$, and the main contribution compared to Wang *et al.*, (2022) is a more detailed investigation of flow around the cylinder. Specifically, the influence of the flapping film at the cylinder free end on the near-wake structure was systematically investigated. Both smoke-wire flow visualization and particle image velocimetry (PIV) measurements were conducted in multiple spanwise planes and the central lateral plane to reveal the near-wake dynamics under the effects of the flapping film. Time-average and phase-average methods were utilized to study the evolution of FIVs and their effects on the wake. FIVs identified through flow visualization and PIV measurements were compared, and the relation between the flapping motion and the development of FIVs was also revealed in great detail.

II. EXPERIMENTAL DETAILS

A. Experimental setup

The experiments were conducted in an open-circuit low-speed wind tunnel with a test section of 1200 mm long, 450 mm high, and 450 mm wide. Freestream velocity U_∞ in the test section can be adjusted continuously from 0 to 40 m/s with a turbulence intensity less than 0.5%. The tested model was a finite square cylinder with $H/d = 5$, where $H = 200$ and $d = 40$ mm are the height and width of the cylinder, respectively. As shown in Figs. 1(a) and 1(c), the cylinder was fixed on a horizontal flat plate with a streamlined leading edge. The width and length of this flat plate were 450 and 1000 mm, respectively. The horizontal plate was approximately 50 mm above the bottom wall of the test section to minimize the effects of the boundary layer on it. The origin of the coordinate system was set at the center of the bottom trailing edge of the testing cylinder, as shown in Fig. 1(a). Particularly, x, y, and z indicate the streamwise, lateral, and spanwise directions, respectively. The blockage ratio caused by the cylinder was 4%, small enough not to affect the results (Hunt, 1982).

The flexible film was vertically clamped at the leading edge of the cylinder's free end [Figs. 1(a) and 1(c)]. The film was made of low-density polyethylene with a density ρ_s of 0.91 g/cm^3 and a flexural modulus E of 240 MPa. The flexible film was 0.04 mm in thickness and 40 mm in width, identical to d [Fig. 1(a)]. The length l of the film was also 40 mm, i.e., the dimensionless length $l^* = 1$. The superscript * in the present paper indicates the normalization using d and/or U_∞.

B. Oncoming flow conditions

The square cylinder was located 0.4 m downstream from the leading edge of the flat plate. The boundary layer condition over the

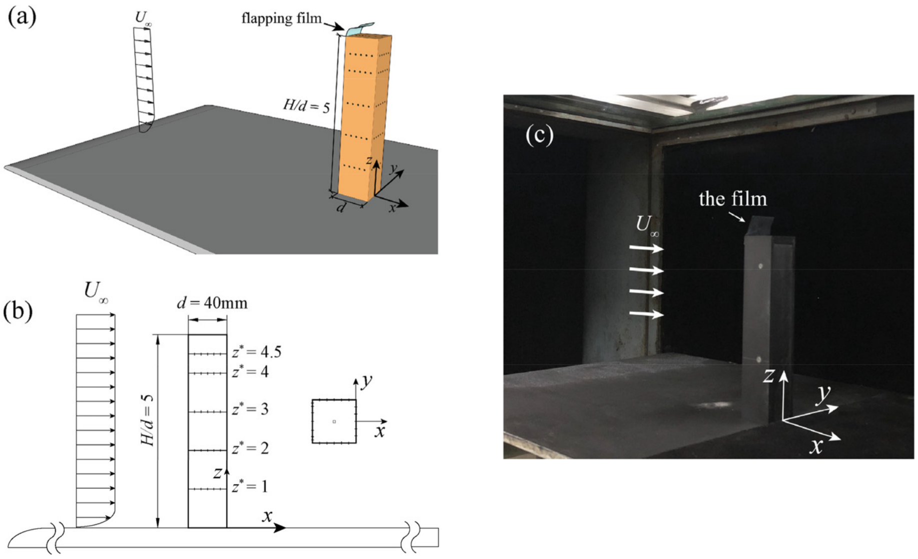

FIG. 1. Experimental setup and coordinate system: (a) sketch of the setup, (b) arrangement of pressure taps, and (c) actual picture of the setup.

plate was documented using a Cobra probe (TFI, Series 100) along the z axis prior to the model installation. The documentation was conducted at $U_\infty = 5$, 10, and 15 m/s. The Cobra probe was fixed on a 3D traverse system with an accuracy of 0.01 mm in each direction. The sampling frequency was 2 kHz, and the sampling duration was 20 s at each measurement point. Figure 2 presents the profile of the normalized time-averaged streamwise velocity $\overline{U^*}$ and the streamwise turbulence intensity I_{uu} at different U_∞. The distributions of $\overline{U^*}$ and I_{uu} agree well with each other for the three U_∞, suggesting that the boundary layer over the plate was fully developed. The boundary layer thickness is about 0.4 *d*, as shown in Fig. 2, which means the majority of the cylinder is in a uniform flow.

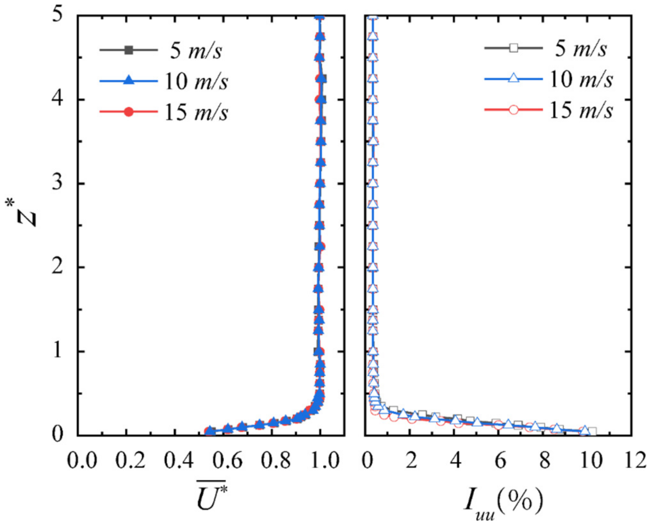

FIG. 2. Boundary layer conditions on the flat plate at $U_\infty = 5$, 10, and 15 m/s.

C. Measurement techniques

1. Measurement of aerodynamic forces

The effects of the flexible film at the free-end leading edge on the aerodynamic forces of the finite square cylinder of $H/d = 5$ were studied in our previous investigation (Wang *et al.*, 2022). It was found that the flapping film reduces the aerodynamic forces of the cylinder remarkably, which is almost independent of l^* and U_∞. Figure 1(b) presents the arrangement of pressure taps, which is identical to Noda and Nakayama (2003), Wang *et al.*, (2017, 2022) and Zhao *et al.* (2021). Pressure taps were placed around the cylinder at $z^* = 1$, 2, 3, 4, and 4.5. There were 22 taps at each height, including 7 on the windward face and the rest 15 evenly arranged on the lateral and leeward faces. The additional drag induced by the flapping film can be negligible in the present study, as confirmed by Wang *et al.* (2022). The pressure tubes, connecting the taps and pressure scanner (DTC Initium), were 300 mm long with an inner diameter of 0.8 mm. The maximum uncertainty of the pressure scanner is about ±0.1% of full scale pressure range (2.4 Pa). The sampling frequency of pressure scanners was 333 Hz/channel, and the sampling duration was 150 s for each case.

Three aerodynamic force coefficients, i.e., time-averaged drag coefficient $\overline{C_d}$, fluctuating drag coefficient C_d', and fluctuating lateral force coefficient C_l', are defined as

$$\overline{C_d} = \frac{\overline{F_d}}{\frac{1}{2}\rho_f U_\infty^2 A}, \quad C'_d = \frac{F'_d}{\frac{1}{2}\rho_f U_\infty^2 A}, \quad \text{and} \quad C'_l = \frac{F'_l}{\frac{1}{2}\rho_f U_\infty^2 A}, \tag{1}$$

where the time-average drag $\overline{F_d}$, the fluctuating drag force F_d', and the fluctuating lateral force F_l' are calculated through pressure integration (neglecting viscous drag). $A = H{\cdot}d$ is the projected area of the tested cylinder in the cross-stream direction, and ρ_f is the air density.

2. Measurement of near-wake flow

Since the reduction of aerodynamic forces is insensitive to U_∞ (Wang *et al.*, 2022), the near-wake measurement was only performed at $U_\infty = 5$ m/s in the present study, corresponding to the Reynolds number of 13 700. Both smoke-wire flow visualization and PIV measurements were conducted in the lateral central plane at $y^* = 0$ and 14 horizontal planes from $z^* = 1.5$ to 6, as shown in Fig. 3. As a classic technique for flow visualization, smoke wire is commonly used in wind tunnel experiments due to its convenience, economy, and flexibility (Yarusevych *et al.*, 2009). In the present study, a smoke-wire generator (Model: Hanghua SW) was used for flow visualization. Paraffin oil was brushed on the thin stainless wire with a diameter of 0.1 mm to generate tracing smoke. The stainless wire was mounted 8 cm upstream the cylinder. Because of surface tension effects, the paraffin oil turned into evenly distributed droplets of about 0.2 mm in diameter. Two capacitors of 200 V were used to generate a powerful transient current of about 20 A through the wire. The heated wire gasified the paraffin droplets on it, generating thin tracing smoke.

A 2D PIV was also employed to measure the near-wake flow fields in the planes as shown in Fig. 3 using an ANDOR Zyla sCMOS camera operated at 5 Hz. The resolution of the sCMOS camera was 2560×2160 pixel^2. The laser sheet was approximately 2 mm thick, produced by a 380 mJ Beamtech Vlite-380 double-pulsed laser. The wavelength of the laser is 532 nm, and each pulse lasted for 6–9 ns. The synchronization among the laser triggering and the image taking was realized by the IDT USB timing hub XS-TH. In each measurement plane, 2000 instantaneous snapshots were captured for the analysis. The interval between two successive images was 50 μs for all measurements that the particles would travel only around 0.25 mm ($\approx$0.006 d) at $U_\infty = 5$ m/s. Tracing particles used in PIV experiments were atomized paraffin oil with an average diameter of about 3 μm generated by a pressure nozzle. The spatial resolution of the present PIV measurement was 112 μm/pixel. The interrogation window used in the cross correlation algorithm was 32×32 pixel^2 with a 50% overlap in both directions. Accordingly, the real size of the interrogation window was 3.58×3.58 mm^2 (approximately 0.09 $d \times 0.09$ d), corresponding to the velocity vector fields with 159×134 vectors, which could be assumed fine enough to capture the large-scale flow structures in the cylinder near wake. The uncertainty analysis for the PIV measurement was conducted using the image-matching methodology by software Dynamic Studio, as described in Sciacchitano *et al.* (2013). The maximum uncertainty for both velocity components was found to be less than 2% of the mean velocity. Although flow near the free end is highly three-dimensional, where particles could pass through the laser sheet leading to a lower correlation between two successive images because of perspective projection effects, but because of the relatively low out-of-plane velocity [about one third of U_∞ in the vertical and twice of U_∞ in the horizontal, Wang and Zhou (2009)] of flow in this area, the correlation would be reliable where most of the particles would stay in the laser sheet.

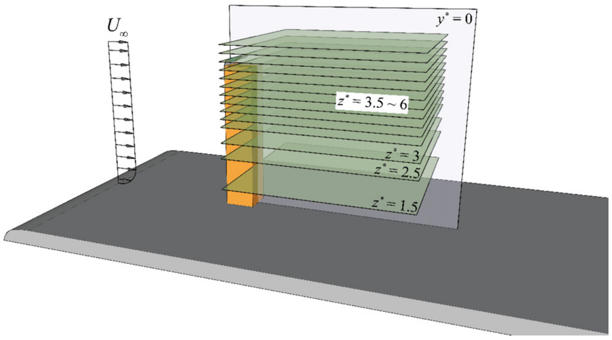

FIG. 3. Arrangement of flow visualization and PIV measurement planes.

3. Phase average technique

Considering that the flexible film flaps periodically at $U_\infty = 5$ m/s, the phase average technique is applied to reveal the flapping-induced vortices, i.e., FIVs, in the near wake, similar to that used in Bourgeois *et al.*, (2011), Lyn and Rodi (1994), and Sattari *et al.* (2012). Using the phase average technique, an instantaneous variable, $v(t)$, can be decomposed into a phase-varying component, $\langle v \rangle$, and a residual v'. The phase-varying component $\langle v \rangle$ can be further decomposed into a time-averaged component $\overline{v}$ and a periodic component $\tilde{v}$ with a zero mean value, resulting in the triple decomposition

$$v(t) = \langle v \rangle + v' = \overline{v} + \tilde{v} + v' \tag{2}$$

Different from the Reynolds decomposition, triple decomposition is also an averaging method but performed for certain phases rather than over the entire sampling record. The reference signal determining the phase angle is crucial for phase-average analysis (Lyn and Rodi, 1994). Considering that the fluctuating pressure on the cylinder free end associates well with the flapping motion of the flexible film (Wang *et al.*, 2022), it is used as the reference signal in the present study. To this end, a pressure-image synchronization system was set up as shown in Fig. 4, with an AD board simultaneously sampling the triggering signal of PIV and the fluctuating pressure on the cylinder free end.

The fluctuating pressure on the free end of the cylinder is presented in Fig. 5 as a gray curve. The pressure was measured using a pressure transducer (Model: CYY4 Xi'an aviation instruments), and the sampling frequency is 2000 Hz. The uncertainty of the pressure transducer is 0.1% of full scale pressure range (3 Pa), which is accurate enough to capture the pressure variation and figure out the periodicity of the flapping film as seen in Fig. 5. The flapping frequency of the film at $U_\infty = 5$ m/s was 29 Hz. Accordingly, the pressure signal was bandpass filtered, reserving the components of frequency within 29 $\pm$ 2 Hz, as shown by the red line in Fig. 5. Obviously, both the raw and the bandpass filtered signals exhibit a marked periodicity, with a negligible phase shift between them. As shown in Fig. 5, critical phase points, i.e., $\Phi = 0$, $\pi/2$, π, and $3\pi/2$, were recognized based on the filtered signal, identical to that used by Hussain and Hayakawa (1987), Lou *et al.*, (2016), and Zhou and Yiu (2006). Subsequently, each cycle was divided into 20 phase bins. The instantaneous PIV-measured flow fields, corresponding to the triggering signal shown by the blue line in Fig. 5, can be sorted into these specific phase bins. In each measurement plane, a total of 2000 random snapshots ensured that there were approximately 100 samples in each phase bin for the phase-average analysis.

III. RESULT AND DISCUSSION

A. Aerodynamic forces

Since more details about aerodynamic forces can be found in Wang *et al.* (2022), only a short description is included here. Aerodynamic forces of the cylinder were estimated by integrating the

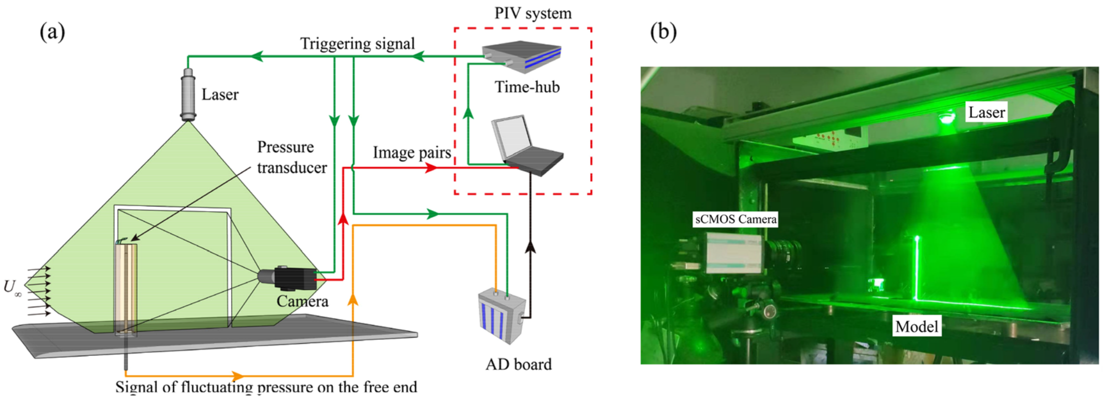

FIG. 4. (a) Schematic of the pressure-image synchronization system and (b) setup of PIV.

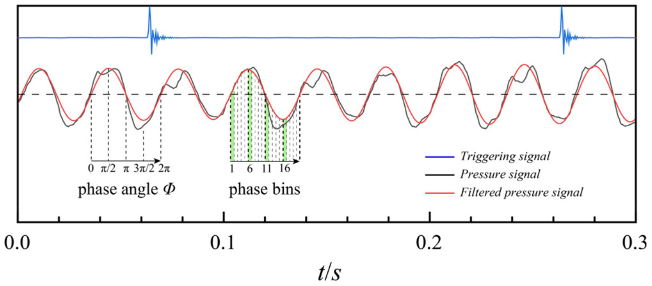

FIG. 5. Time histories of the raw and filtered pressure signals, and the triggering signal of PIV.

pressure as discussed in Wang *et al.* (2022). Figure 6 depicts the dependence of $\overline{C_d}$, C_d', and C_l' on U_∞ for the finite cylinder with and without the flexible film. For the bare cylinder, i.e., $l^* = 0$, $\overline{C_d}$, C_d', and C_l' are 1.65, 0.06, and 0.12, respectively, independent of U_∞ increasing from 4 to 20 m/s. These forces are reduced by about 5%, 25%, and 60%, respectively, once the flexible film with $l^* = 1$ flaps at its free-end leading edge (Fig. 6). Wang *et al.* (2022) suggested that once the flexible film flaps at $U_\infty > U_c$, the reduction in the aerodynamic forces is insensitive to both l^* and U_∞. Interested readers may refer to our previous publication (Wang *et al.*, 2022) for more details about the behaviors of the aerodynamic forces under the effects of the flapping film. In the following discussion of the present paper, only the results for $l^* = 1$ and $U_\infty = 5$ m/s will be studied in detail to reveal the mechanism of the force reduction induced by the flapping film.

B. Flapping configurations of the flexible film

Prior to further discussions on the wake structure, it is necessary to discuss the flapping behavior of the flexible film. To do this, long exposure photography was employed for the film with $l^* = 1$ at $U_\infty = 5$ m/s. The flapping film was illuminated by continuous and pulsing lasers as shown in Figs. 7(a) and 7(b), respectively.

The envelope of the flapping film is clearly observed in Fig. 7(a), which touches the free end at approximately 0.7*d* downstream of the leading edge. Similar to that observed by Leclercq *et al.* (2018), the film is more curved during the upward stroke than the downward stroke, as shown in Fig. 7(b). Consequently, the trajectory of the trailing end of the flapping film forms a teardrop shape curve, bending upstream at its upper part (Fig. 7).

As a complement of the phase-average analysis of the wake, the correlation between flapping configurations and fluctuating pressure on the cylinder free end can be determined, as shown in Fig. 8. The tip

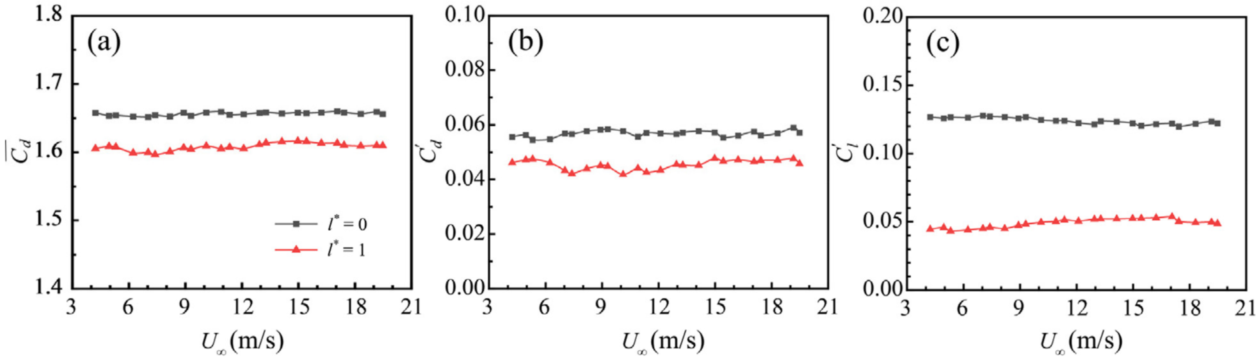

FIG. 6. Aerodynamic forces of the finite square cylinder: (a) $\overline{C_d}$, (b) C_d', and (c) C_l'.

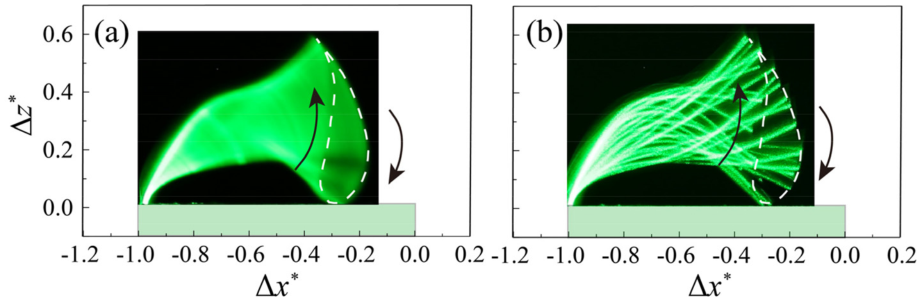

FIG. 7. Visualization of the film configurations using long exposure, illuminated with (a) continuous laser and (b) pulsing laser.

of the film starts flapping downwards at phase 1, moves toward the free end at phase 6, and touches the free end before flapping upwards at phase 11. The middle part of the film reaches the highest point at phase 16. After that, the trailing end of the film reaches its highest position again at phase 1, starting a new cycle. More details can be found in Wang *et al.* (2022). In addition, the flapping frequency of the film is linearly related to the wind velocity and is always higher than the vortex shedding frequency, as reported in Wang *et al.* (2022).

C. Near-wake structures

1. *Flow visualization results*

Figures 9(a) and 9(b) present the results of flow visualization in the central lateral plane, i.e., at $y^* = 0$, for the cases with $l^* = 0$ and 1, respectively. The free-end shear flow in the uncontrolled case [Fig. 9(a)] is laminar and smooth immediately after the separation, followed by the Kelvin–Helmholtz (K–H) vortices downstream. This free-end shear flow bends down gradually because of the downwash flow and tip vortices (Wang and Zhou, 2009). As shown in Fig. 9(a), no large-scale periodic vortices appear in the free-end shear flow, in line with that reported by Uffinger *et al.* (2013) and Wang and Zhou (2009). Contrarily, for the controlled case with $l^* = 1$ [Fig. 9(b)], strong large-scale FIVs appear in the shear flow. Compared with the uncontrolled case [Fig. 9(a)], FIVs enhance the momentum transport between the freestream and the near wake, by introducing more high-speed fluid into the wake, as marked by the arrows in Fig. 9(b).

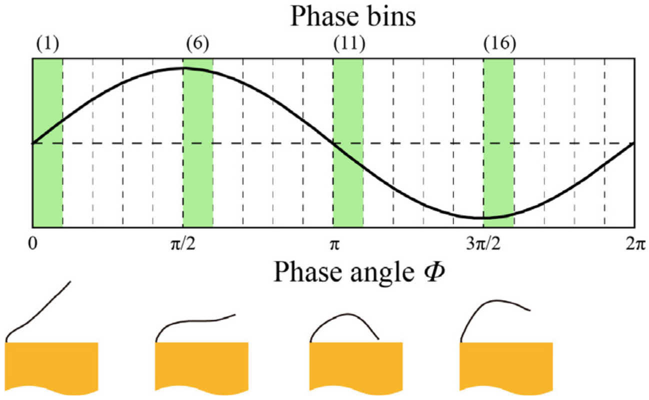

FIG. 8. Diagram of the phase indicator, i.e., filtered pressure on the free end, definition of phases, and corresponding instantaneous configurations of the flapping film at phases 1, 6, 11, and 16.

This enhanced momentum exchange results in a significant change in the near-wake structures, which will be addressed in detail later.

The flapping motion and the corresponding downstream evolution of FIVs in a typical cycle are presented in Fig. 10. The snapshot in Fig. 10(a) corresponds to the moment when the flexible film is at its lowest position and starts to flap upwards. The flexible film lifts the free-end shear layer gradually when flapping upwards, as shown in Figs. 10(a)–10(d). The elevated shear layer bends down significantly when flowing over the flexible film, forming an obvious vortex behind the film [Fig. 10(d)]. Compared to the bare cylinder case, the downward bending of the free-end shear flow is more discernible because of the strong negative pressure on the free end, induced by the flexible

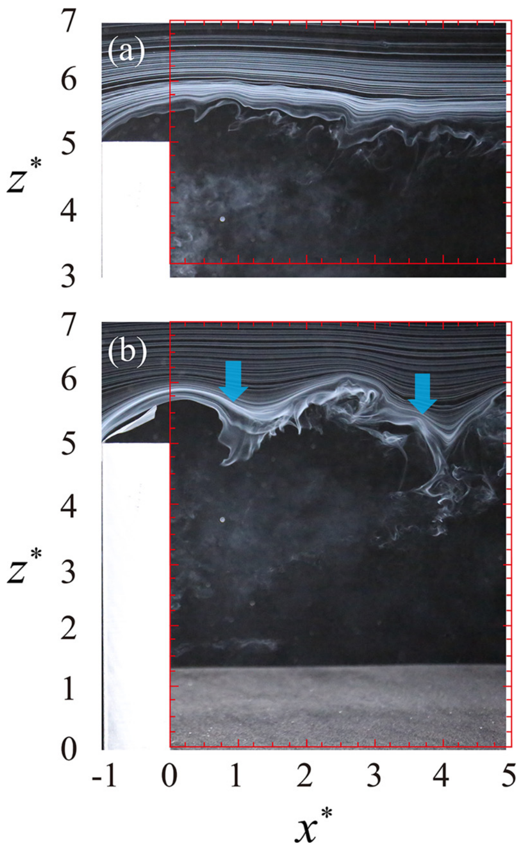

FIG. 9. Flow visualization in the central lateral plane: (a) $l^* = 0$ and (b) $l^* = 1$.

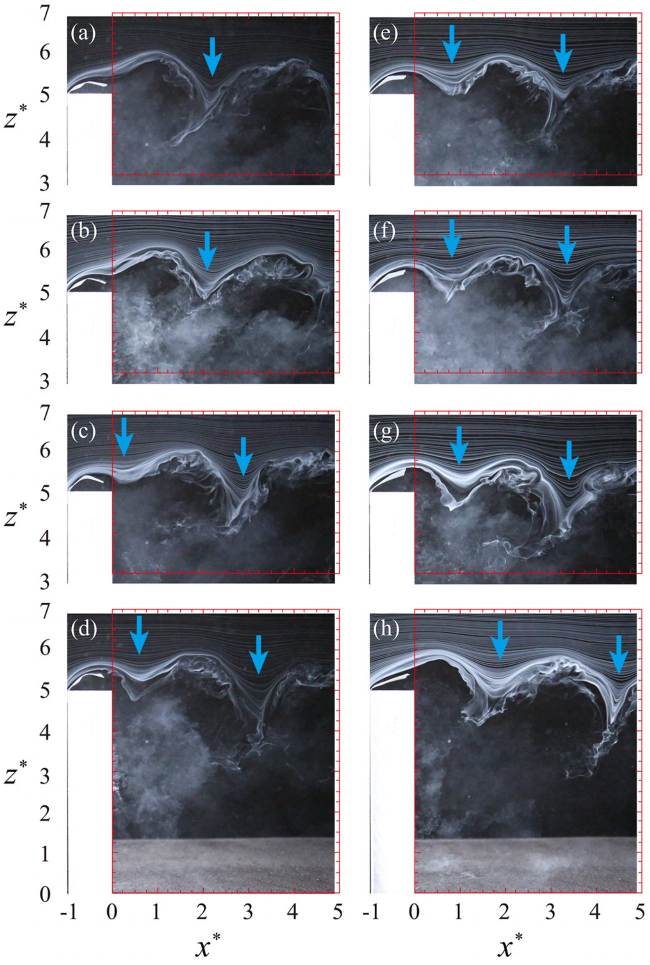

FIG. 10. Flow visualization in one flapping cycle for the case of $l^* = 1$.

film when it flaps upwards; see Fig. 8 of Wang *et al.* (2022) for reference. The FIV enlarges gradually during the downward flapping stroke of the film and matures when the film approaches its lowest position, as shown in Figs. 10(e)–10(h). After that, the film flaps upwards, repeating the process in the subsequent cycle. The flow between the FIVs impacts the recirculation region behind the cylinder, which extends downwards to $z^* \approx 3$, as presented in Figs. 9 and 10, and is far stronger than the effects of the downwash flow on the wake of the bare cylinder.

Flow visualization snapshots in horizontal planes at different z^* are presented in Fig. 11. For the uncontrolled case, the cylinder has a negligibly small impact on the flow over the free end of the cylinder at $z^* = 5.5$. The streamlines at this level are mainly parallel to each other. On the other hand, an obvious convergence appears at $z^* = 5.5$ for the controlled case, as highlighted by the blue arrow in Fig. 11. This convergence is attributed to the downwash flow generated by the flapping-induced vortices (FIVs), as depicted in Figs. 9 and 10. This observation becomes even more significant in the plane at $z^* = 5$, where a distinct pattern of alternating divergence and convergence of streamlines is observed in the controlled case. In contrast, the uncontrolled case is characterized by primarily converged streamlines.

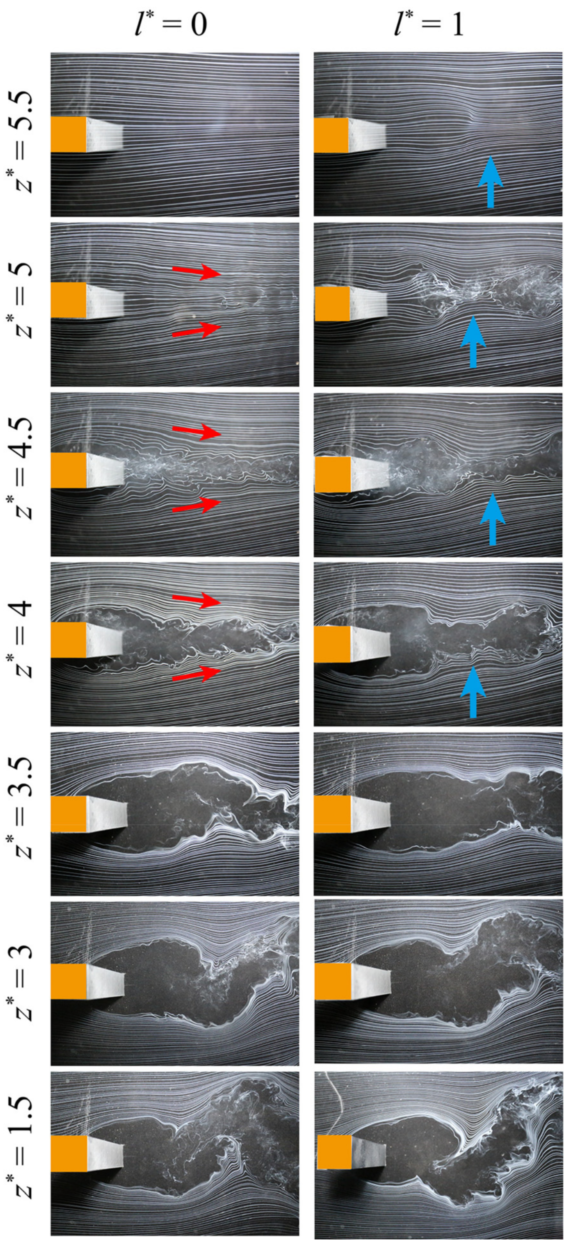

FIG. 11. Flow visualization results for the uncontrolled case with $l^* = 0$ (left) and controlled case with $l^* = 1$ (right) in horizontal planes from $z^* = 1.5$ to 5.5 at $U_\infty = 5$ m/s.

In the planes slightly lower than the free end, i.e., $z^* = 4.5$ and 4, for $l^* = 0$, the spanwise shear flow, characterized by small-scale K–H vortices, converges gradually when moving downstream, as marked with red arrows in Fig. 11. For the case with $l^* = 1$, large-scale symmetrical spanwise vortices dominate the near wake. This flow visualization suggests that the flapping film not only induces FIVs in the lateral plane but also converts the spanwise shear flow near the cylinder free end into large-scale symmetrical vortices.

In the lower spanwise plane at $z^* = 3.5$, the near wake is characterized by a zigzag flow in the uncontrolled case. This zigzag structure is less obvious in the controlled case. Moreover, the near wake is much wider for the latter. As observed in Figs. 9 and 10, FIVs impact on the recirculation zone at $z^* = 3.5$, which explains the widening of the wake and suppression of alternating spanwise vortices, as shown in Fig. 11. It is worth mentioning that, based on their pressure measurement results, Wang *et al.* (2022) suggested that alternating spanwise vortices are also attenuated at $z^* \leq 3.5$. However, the effect of the flapping film on the near-wake flow at $z^* \leq 3.5$ is not that obvious in the present flow visualization result (Fig. 11), which suggests the necessity of a more detailed quantitative analysis.

2. PIV measurements

Both time-averaged and phase-averaged PIV results are studied systematically to quantitatively reveal the effects of FIVs on the near wake. Figure 12 presents the iso-surface of $\overline{U^*} = 0$ (red-bold line), i.e., the boundary of the mean recirculation region, in the cylinder wake, which is reconstructed from the PIV results in the spanwise planes shown in Fig. 3. In addition, the contours of $\overline{U^*}$ overlapped with the mean streamlines in the central lateral plane are also presented. Note that the results in the central lateral plane are shifted to $y^* = 3$ for easy data interpretation.

For the uncontrolled case, the maximum streamwise extent of the recirculation region reaches $x^* = 2.75$ in the lower part of the wake, which agrees well with the contour $\overline{U^*} = 0$ in the central lateral plane as in Sumner *et al.* (2017), Wang *et al.* (2006), Wang and Zhou (2009), Zhao *et al.* (2021), and Wang *et al.* (2020). The streamwise extent remains almost the same in the lower part $z^* < 2.5$, whereas it gradually shrinks toward the free end, obviously caused by the free-end downwash flow, presented by the streamlines in the lateral plane.

As for the controlled case, the flapping film exerts a significant effect on the near wake as shown in Fig. 12(b). An obvious crater appears in the iso-surface of the recirculation region near the free end, caused by the enhanced downwash flow. This observation accords well with the smoke-wire flow visualization results shown in Figs. 9 and 10. That is, the FIVs bring in high-speed fluid from the free stream into the wake, suppressing the recirculation region near the free end. Contrarily, the recirculation region in the lower half of the wake extends further downstream, reaching $x^* = 3.60$ at $z^* = 1.5$, approximately 30% larger than the uncontrolled case. According to the result in the central plane, the streamwise extent of the recirculation region becomes almost unchanged at $z^* < 2$, significantly lower than that of the uncontrolled case. It can be confirmed that the effects of the FIVs are not confined near the free end but appear on the entire cylinder wake.

It is interesting to reveal the detailed near-wake structure modulated by the flapping film, which is essential for understanding the mechanism of the enhanced momentum transport caused by the FIVs. Figure 13 presents the phase-averaged dimensionless lateral vorticity $\tilde{\omega}_y^*$, the dimensionless streamwise velocity $\tilde{u}^*$ in the central lateral plane, and the dimensionless spanwise vorticity $\tilde{\omega}_z^*$ in the horizontal plane at $z^* = 5$. All results are overlapped with the corresponding phase-averaged streamlines. Definitions of phases 1, 6, 11, and 16 are given in Fig. 8.

The flexible film generates an alternating vortex row at $z^* \approx 6$ in the central plane during its flapping stroke, as shown in Figs. 13(a), 13(d), 13(g), and 13(j). Particularly, the flapping film forms a positive vortex downstream of its tail when it flaps downwards from its highest position (from phases 1 to 6). This positive vortex detaches completely from the film when the film reaches its lowest position (phase 11). Subsequently, when the film flaps upwards (from phases 11 to 16), a negative vortex grows, which detaches from the film when it arrives at its highest position (phase 1). This process repeats continuously when the film flaps periodically.

Although the foci of the streamlines in the central plane keep approximately unchanged in height as the FIVs detach completely from the film, the contours of $\tilde{u}^*$ extend downwards, i.e., to smaller z^*, gradually as the FIVs develop downstream, as shown in Figs. 13(b), 13(e), 13(h), and 13(k). This observation is also illustrated by the streamlines in the central lateral plane, which point upstream and

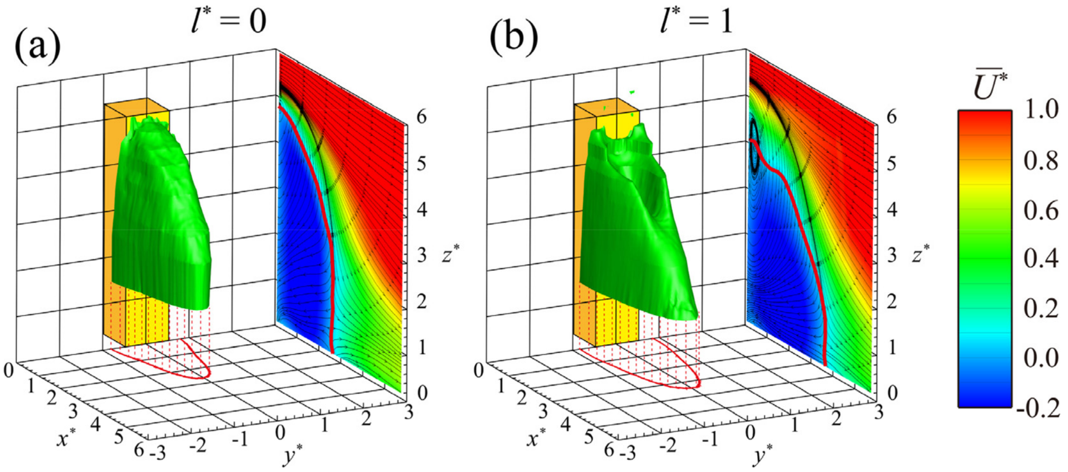

FIG. 12. Time-averaged recirculation region and the contours of $\overline{U^*}$ in the central lateral plane at $U_\infty = 5$ m/s: (a) $l^* = 0$ and (b) $l^* = 1$.

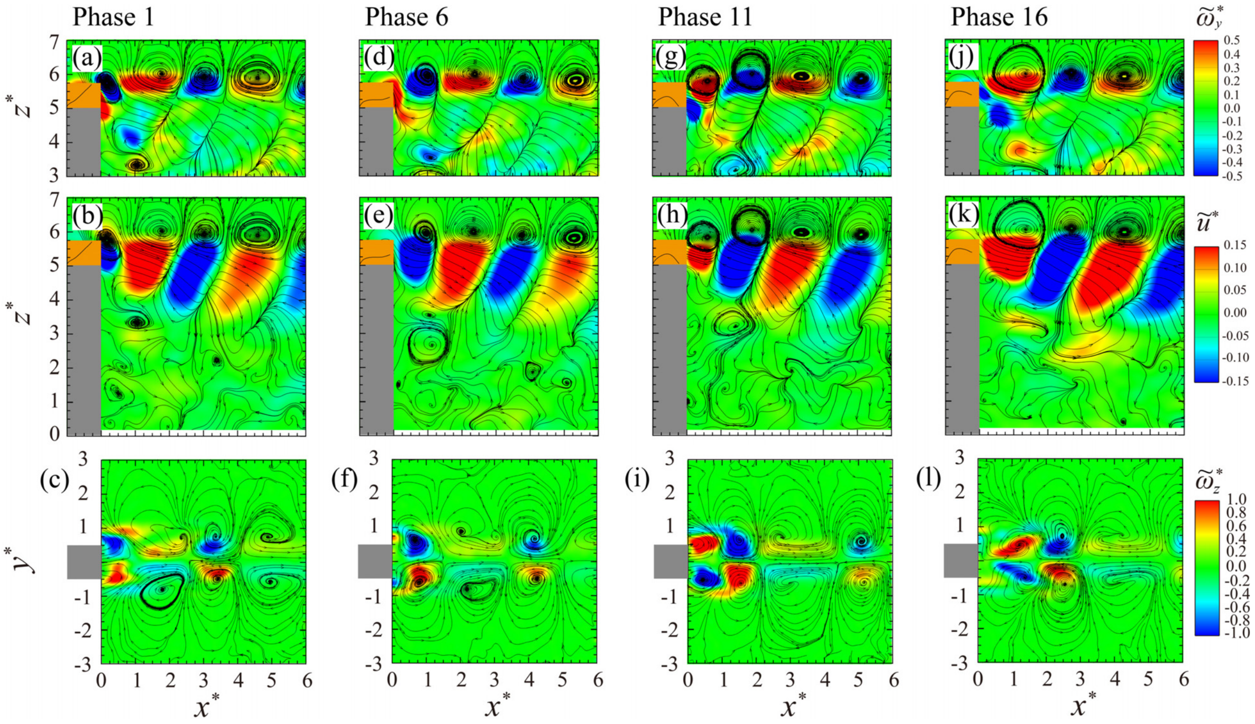

FIG. 13. Contours of phase-averaged $\tilde{\omega}_y^*$ and $\tilde{u}^*$ in the central lateral plane and $\tilde{\omega}_z^*$ in the horizontal plane at $z^* = 5$ for case $l^* = 1$. All contours are overlapped with phase-averaged streamlines. [(a), (d), (g), and (j)] $\tilde{\omega}_y^*$, [(d), (e), (h), and (k)] $\tilde{u}^*$, and [(c), (f), (i), and (l)] $\tilde{\omega}_z^*$.

downstream alternately in the streamwise direction. As revealed by the numerical simulation of Nishiura *et al.* (2019) and Huang and Sung (2010), a flapping flag generates vortices not only from its trailing edge but also from its side edges. The vortical structure shed from the trailing edge connects those from the side edges, forming an n-shaped structure with two legs. Figures 13(c), 13(f), 13(i), and 13(l) present the phase-averaged vorticity and streamlines in the horizontal plane at $z^* = 5$. Symmetrical vortical structures present in this horizontal plane, which are completely associated with the FIVs observed in the central lateral plane. This observation suggests that the present flexible film, which is perpendicular to the oncoming flow at its root, also generates n-shaped structures during its flapping cycle. The vortical structure shed from the trailing edge of the film connects those from side edges, similar to that observed by Huang and Sung (2010) and Nishiura *et al.* (2019). The two legs of this n-shaped vortical structure may extend to an altitude lower than the free end, as revealed by the contours of $\tilde{u}^*$ and the corresponding phase-averaged streamlines shown in Fig. 13.

To understand the wake structure in more detail, Fig. 14 presents the phase-averaged flow structures in different horizontal planes from $z^* = 6$ to 3. Contours of $\tilde{u}^*$, $\tilde{v}^*$, and $\tilde{\omega}_z^*$ at each height are depicted and vertically arranged in Fig. 14. Only the results at phase 1 are given for simplicity. The vortex pairs induced by the flapping film are named V1, V2, and V3, according to their positions in the x direction, as shown in Fig. 14, which are distinguished with green and yellow backgrounds.

Although $\tilde{\omega}_z^*$ at $z^* = 6$ is fairly small compared to that at lower heights, with no distinct vortex pairs, significant segmented flow structures can be observed. The contours of $\tilde{v}^*$ develop in pairs and those of $\tilde{u}^*$ develop one by one with different signs. A single contour of $\tilde{u}^*$ connects the two pairs of $\tilde{v}^*$ contours. Weak $\tilde{\omega}_z^*$ at $z^* = 6$ suggests the feeble contribution of FIVs on vorticity at this height, while the results in plane $y^* = 0$ [Figs. 13(a) and 13(b)] suggest significant FIVs with large $\tilde{\omega}_y^*$. This huge discrepancy implies a very strong three-dimensional effect of FIVs and their limited impact on the flow around the free end.

The $\tilde{\omega}_z^*$ at lower heights, i.e., $z^* = 5.5$, 5, and 4.5, is larger since it gets closer to the flapping film, and obvious vortex pairs can be observed. The $\tilde{\omega}_z^*$ at $z^* = 5$ is stronger that that at $z^* = 5.5$ and 4.5. The distribution of $\tilde{v}^*$ is qualitatively similar at z^* from 6 to 4.5, as shown in Figs. 13(a)–13(d). Contrarily, the contours of $\tilde{u}^*$ at $z^* = 6$ have opposite signs compared to those at low heights. This discrepancy in the signs of $\tilde{u}^*$ suggests that FIVs change their direction in a streamwise direction between $z^* = 6$ and 5.5, where the centers of FIVs are located in the central lateral plane, as shown in Fig. 13. Vortex pairs decay gradually as they develop downstream. For example, the $\tilde{\omega}_z^*$ of V3 is smaller than that of V1 and V2. The distorted streamlines of V3 at $z^* = 5.5$ also suggest the same.

For lower spanwise planes, i.e., $z^* = 4$ and 3, it is hard to distinguish vortex structures from the disordered streamlines and $\tilde{\omega}_z^*$ contours. The value of $\tilde{\omega}_z^*$ at $z^* = 4$ and 3 is generally smaller than that at higher levels, suggesting the weakening of FIVs as approaching the bottom wall. The weakening of $\tilde{u}^*$ and $\tilde{v}^*$ also proves the same. It can thus be concluded that the impact of FIVs is limited in a range from approximately $z^* = 6$ to 4.

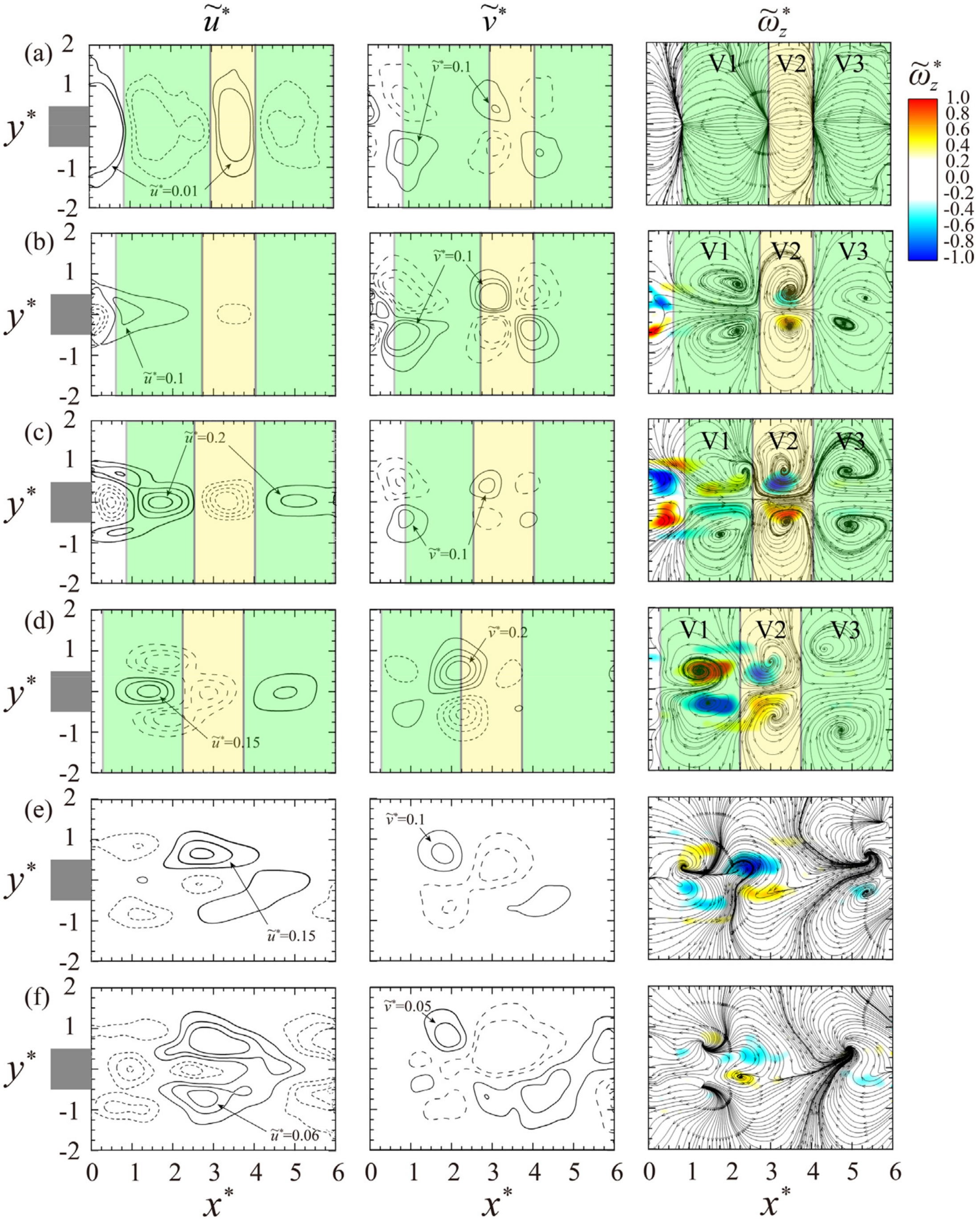

FIG. 14. Contours of phase-averaged $\tilde{\omega}_z^*$, covered with streamlines for case $l^* = 1$ in horizontal planes (a) $z^* = 6$, (b) $z^* = 5.5$, (c) $z^* = 5$, (d) $z^* = 4.5$, (e) $z^* = 4$, and (f) $z^* = 3$ at $U_\infty = 5$ m/s.

Figure 15 shows the oblique development of FIVs as seen in the horizontal streamlines; the thick lines indicate the vortex filaments of the FIVs, which are characterized by the n-shape structure. The red line corresponds to a positive value of $\tilde{\omega}_y^*$ in the central lateral plane at $y^* = 0$. Based on that, a sketch of FIVs is proposed in Fig. 16; from left to right are V1, V2, and V3, respectively, colored in red, blue, and red according to the sign of $\tilde{\omega}_y^*$ in the plane $y^* = 0$. Due to the less organized structures at $z^* < 4$ [Figs. 14(e) and 14(f)], the part of FIVs

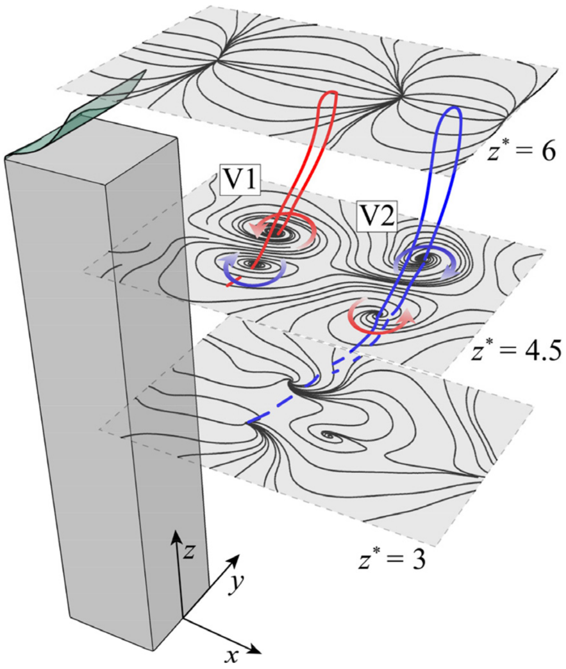

FIG. 15. Phase-averaged streamlines at $z^* = 6$, 4.5, and 3 and associated vortex filaments.

beneath $z^* = 4$ is not included. Similar to vortical structures revealed in Huang and Sung (2010) and Nishiura *et al.* (2019), FIVs in the present study are also n-shaped. Particularly, the vortex from the trailing edge connects those from side edges. The two legs of this n-shaped vortical structure, i.e., the vortices from two side edges, decay gradually with reducing z^*. However, different from O-shaped vortices with a closed tail induced by a flapping flag at a high Reynolds number as reported in Huang and Sung (2010), the two legs from two side edges do not connect with each other at the lower part of the wake because of the presence of the cylinder in the present study.

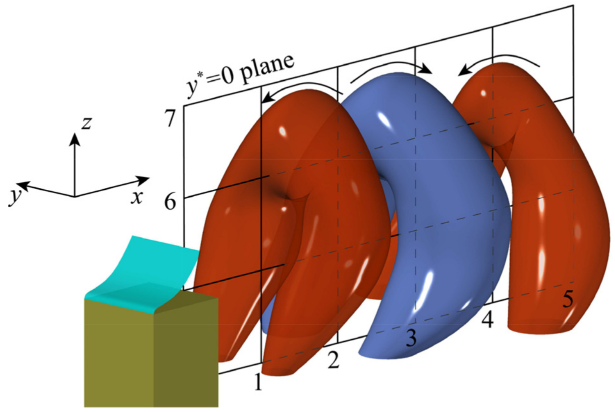

FIG. 16. Illustration of FIVs near the free end in phase 1 for case $l^* = 1$ at $U_\infty = 5$ m/s; the red and blue colors of each branch represent the sign of $\tilde{\omega}_y^*$ in the plane $y^* = 0$.

IV. CONCLUSIONS

As commonly used simplified models for high-rise buildings or towering structures, finite square cylinders are widely employed to do aerodynamic tests and explore a new way for improvements. The present study is a follow-up study of Wang *et al.* (2022), which introduced a novel and efficient flow control method to reduce the aerodynamic forces of a finite square cylinder and explains well the behind mechanism through a series of pressure measurements. The main contribution of the present study is the supplementary explanation of load reduction from the view of flow around the cylinder. The near-wake flow structures of a finite square cylinder with a flapping flexible film at its free-end leading edge were experimentally investigated through flow visualization and PIV measurements. Phase-averaged analyses of PIV results were conducted in the central lateral plane and several horizontal planes near the free end to reveal the characteristics of FIVs. The investigation leads to the following conclusions:

(1) Flow visualization results suggest that FIVs replace the shear flow near the free end, converting small-scale irregular vortices in the free-end shear flow into large-scale regular vortices, i.e., FIVs. For the flow relatively far from the free end, i.e., the flow beneath $z^* = 3.5$, the wake structure is still characterized by alternating Karman vortices.
(2) Under the influence of the flapping film, an obvious crater appears in the iso-surface of the recirculation region, implying the enhancement of the downwash flow allowing the introduction of a high-speed freestream into the wake. The enhanced downwash flow caused by FIVs exhibits a suppression effect on the spanwise flow, leading to a streamwise extension of the recirculation region.
(3) The flapping film produces a row of alternating vortices in the wake. In the central lateral plane, a positive vortex forms when the film flaps downwards from the highest position and it detaches when the film reaches the lowest position. A negative vortex starts to form when the film starts to flap upwards, and it detaches when the film reaches the highest position. Based on the phase-averaged results, the vortex from the trailing edge of the flexible film connects those from its side edges, forming an n-shaped structure.

As a follow-up study of Wang *et al.* (2022), the present study explains the reduction of the cylinder's aerodynamic forces well based on the modifications of the flow around the cylinder caused by FIVs. Normally, the aerodynamic load acting on an object is closely related to the flow nearby like the discussion in Ranjbar *et al.* (2021); the efficiency of a vertical axis wind turbine changes with the development of vortices near the blades. However, in the present study, the connection between the aerodynamic forces, especially the lateral force, and the development of FIVs is still unclear. Although FIVs dominate the flow near the free end and suppress the spanwise vortices significantly, aerodynamic loads on the square cylinder are still mainly generated by the spanwise vortices as concluded in Wang *et al.* (2022). However, because of the frequency discrepancies among the spanwise vortices and FIVs, connections between the aerodynamic loads and the development of FIVs cannot be built through phase-average method in the present study.

ACKNOWLEDGMENTS

The authors wish to acknowledge the support given to them by the National Natural Science Foundation of China through

Grant No. 52078505 and the Provincial Natural Science Foundation of Hunan (No. 2022JJ30736).

AUTHOR DECLARATIONS

Conflict of Interest

The authors have no conflicts to disclose.

Author Contributions

Chongyu Zhao: data curation (equal); formal analysis (equal); investigation (equal); methodology (equal); validation (equal); visualization (equal); writing—original draft (equal); and writing—review and editing (equal). **Hanfeng Wang:** conceptualization (equal); formal analysis (equal); funding acquisition (equal); methodology (equal); project administration (equal); resources (equal); supervision (equal); writing—original draft (equal); and writing—review and editing (equal). **Zhiwei Liu:** writing—original draft (equal) and writing—review and editing (equal). **Alam Md. Mahbub:** writing—original draft (equal) and writing—review and editing (equal). **Hui Tang:** writing—original draft (equal) and writing—review and editing (equal).

DATA AVAILABILITY

The data that support the findings of this study are available from the corresponding author upon reasonable request.

REFERENCES

Ameya, V. H., Parasuram, I. V. L. N., Supradeenpan, K., and Gurugubelli, P. S., "Effect of material property variation on the dynamic response of a flexible splitter plate attached behind a square cylinder due to flow induced loads," Mater. Today: Proc. **28**(2), 480–485 (2020).

Amini, Y. and Habibi, S. E., "Effects of multiple flexible vortex generators on the hydrothermal characteristics of a rectangular channel," Int. J. Therm. Sci. **175**, 107454 (2022).

Bourgeois, J. A., Sattari, P., and Martinuzzi, R. J., "Alternating half-loop shedding in the turbulent wake of a finite surface-mounted square cylinder with a thin boundary layer," Phys. Fluids **23**(9), 095101 (2011).

Bourgeois, J. A., Sattari, P., and Martinuzzi, R. J., "Coherent vortical and straining structures in the finite wall-mounted square cylinder wake," Int. J. Heat Fluid Flow **35**, 130–140 (2012).

Brücker, C. and Weidner, C., "Influence of self-adaptive hairy flaps on the stall delay of an airfoil in ramp-up motion," J. Fluids Struct. **47**, 31–40 (2014).

Chen, Y. J., Ryu, J., Liu, Y. Z., and Sung, H. J., "Flapping dynamics of vertically clamped three-dimensional flexible flags in a Poiseuille flow," Phys. Fluids **32**, 071905 (2020).

Cui, G. P., Feng, L. H., and Hu, Y. W., "Flow-induced vibration control of a circular cylinder by using flexible and rigid splitter plates," Ocean Eng. **249**, 110939 (2022).

Cui, G. P. and Feng, L. H., "Suppression of vortex-induced vibration of a circular cylinder by a finite-span flexible splitter plate," Phys. Rev. Fluids **7**(2), 024708 (2022).

Fang, Z., Gong, C., Revell, A., Harwood, A., and O'Connor, J., "Passive separation control of a NACA0012 airfoil via a flexible flap," Phys. Fluids **31**(10), 101914 (2019).

Huang, W.-X. and Sung, H. J., "Three-dimensional simulation of a flapping flag in a uniform flow," J. Fluid Mech. **653**, 301–336 (2010).

Hunt, A., "Wind-tunnel measurements of surface pressures on cubic building models at several scales," J. Wind Eng. Ind. Aerodyn. **10**(2), 137–163 (1982).

Hussain, A. K. M. F. and Hayakawa, M., "Eduction of large-scale organized structures in a turbulent plane wake," J. Fluid Mech. **180**, 193–229 (1987).

Jin, Y., Kim, J. T., Hong, L., and Chamorro, L. P., "Flow-induced oscillations of low-aspect-ratio flexible plates with various tip geometries," Phys. Fluids **30**(9), 097102 (2018a).

Jin, Y., Kim, J. T., Mao, Z., and Chamorro, L. P., "On the couple dynamics of wall-mounted flexible plates in tandem," J. Fluid Mech. **852**, R2 (2018b).

Joshi, R. U., Soti, A. K., and Bhardwaj, R., "Numerical study of heat transfer enhancement by deformable twin plates in laminar heated channel flow," Comput. Therm. Sci. **7**(5–6), 467–476 (2015).

Kikuchi, H., Tamura, Y., Ueda, H., and Hibi, K., "Dynamic wind pressures acting on a tall building model—Proper orthogonal decomposition," J. Wind Eng. Ind. Aerodyn. **69–71**, 631–646 (1997).

Kim, Y. C., Bandi, E. K., Yoshida, A., and Tamura, Y., "Response characteristics of super-tall buildings—Effects of number of sides and helical angle," J. Wind Eng. Ind. Aerodyn. **145**, 252–262 (2015).

Kim, S. and Alam, M. M., "Characteristics and suppression of flow-induced vibrations of two side-by-side circular cylinders," J. Fluids Struct. **54**, 629–642 (2015).

Kindree, M. G., Shahroodi, M., and Martinuzzi, R. J., "Low-frequency dynamics in the turbulent wake of cantilevered square and circular cylinders protruding a thin laminar boundary layer," Exp. Fluids **59**(12), 186 (2018).

Kumar, D., Arekar, A. N., and Poddar, K., "The dynamics of flow-induced flutter of a thin flexible sheet," Phys. Fluid **33**(3), 034131 (2021).

Leclercq, T., Peake, N., and de Langre, E., "Does flutter prevent drag reduction by reconfiguration?" Proc. R. Soc. A **474**(2209), 20170678 (2018).

Lee, J. B., Park, S. G., Kim, B., Ryu, J., and Sung, H. J., "Heat transfer enhancement by flexible flags clamped vertically in a Poiseuille channel flow," Int. J. Heat Mass Transfer **107**, 391–402 (2017).

Lee, J. B., Park, S. G., and Sung, H. J., "Heat transfer enhancement by asymmetrically clamped flexible flags in a channel flow," Int. J. Heat Mass Transfer **116**, 1003–1015 (2018).

Li, Y., Li, S. Q., Zeng, L. W., and Wang, H. F., "Control of the VIV of a cantilevered square cylinder with free-end suction," Wind Struct. **29**(1), 77–86 (2019), see http://www.techno-press.org/content/page=article&journal=was&volume=29&num=1&ordernum=8.

Li, S. Q., Luo, Z. B., Deng, X., Peng, W. Q., and Liu, Z. Y., "Experimental investigation on active control of flow around a finite-length square cylinder using dual synthetic jet," J. Wind Eng. Ind. Aerodyn. **210**, 104519 (2021).

Liang, S., Wang, J., Xu, B., Wu, W., and Lin, K., "Vortex-induced vibration and structure instability for a circular cylinder with flexible splitter plates," J. Wind Eng. Ind. Aerodyn. **174**, 200–209 (2018).

Lou, X., Zhou, T., Zhou, Y., Wang, H., and Cheng, L., "Experimental investigation on wake characteristics behind a yawed square cylinder," J. Fluids Struct. **61**, 274–294 (2016).

Lyn, D. A. and Rodi, W., "The flapping shear layer formed by flow separation from the forward corner of a square cylinder," J. Fluid Mech. **267**, 353–376 (1994).

Mao, Q., Liu, Y. Z., and Sung, H. J., "Drag reduction by flapping a flexible filament behind a stationary cylinder," Phys. Fluids **34**(8), 087123 (2022).

Mao, Q., Liu, Y. Z., and Sung, H. J., "Drag reduction by flapping a pair of flexible filaments behind a cylinder," Phys. Fluids **35**(3), 3033602 (2023).

Maruta, E., Kanda, M., and Sato, J., "Effects on surface roughness for wind pressure on glass and cladding of buildings," J. Wind Eng. Ind. Aerodyn. **74–76**(98), 651–663 (1998).

Mashhadi, A., Sohankar, A., and Alam, M. M., "Flow over rectangular cylinder: Effects of cylinder aspect ratio and Reynolds number," Int. J. Mech. Sci. **195**, 106264 (2021).

McClean, J. F. and Sumner, D., "An experimental investigation of aspect ratio and incidence angle effects for the flow around surface-mounted finite-height square prisms," J. Fluids Eng. **136**, 081206 (2014).

Menicovich, D., Lander, D., Vollen, J., Amitay, M., Letchford, C., and Dyson, A., "Improving aerodynamic performance of tall buildings using fluid based aerodynamic modification," J. Wind Eng. Ind. Aerodyn. **133**, 263–273 (2014).

Mooneghi, M. A. and Kargarmoakhar, R., "Aerodynamic mitigation and shape optimization of buildings: Review," J. Build. Eng. **6**, 225–235 (2016).

Nishiura, K., Nishio, Y., Izawa, S., and Fukunishi, Y., "Flapping motion of a permeable flag in uniform flow," Fluid Dyn. Res. **51**(2), 025506 (2019).

Niu, J. and Hu, D. L., "Drag reduction of a hairy disk," Phys. Fluids **23**(10), 101701 (2011).

Noda, H. and Nakayama, A., "Free-stream turbulence effects on the instantaneous pressure and forces on cylinders of rectangular cross section," Exp. Fluids **34**(3), 332–344 (2003).

Park, C. W. and Lee, S. J., "Effects of free-end corner shape on flow structure around a finite cylinder," J. Fluids Struct. **19**(2), 141–158 (2004).

Peng, S., Wang, H., Zeng, L., and He, X., "Low-frequency dynamics of the flow around a finite-length square cylinder," Exp. Therm. Fluid Sci. **109**, 109877 (2019).

Ranjbar, M. H., Rafier, B., Nasrazadani, S. A., Gharali, K., Soltani, M., AI-Haq, A., and Nathwani, J., "Power enhancement of a vertical axis wind turbine equipped with an improved duct," Energy **14**, 5780 (2021).

Rastan, M. R., Sohankar, A., and Alam, M. M., "Low-Reynolds-number flow around a wall-mounted square cylinder: Flow structures and onset of vortex shedding," Phys. Fluids **29**, 103601 (2017).

Rastan, M. R., Sohankar, A., Doolan, C., Moreau, D., Shirani, E., and Alam, M. M., "Controlled flow over a finite square cylinder using suction and blowing," Int. J. Mech. Sci. **156**, 410–434 (2019).

Rastan, M. R., Shahbazi, H., Sohankar, A., Alam, M. M., and Zhou, Y., "The wake of a wall-mounted rectangular cylinder: Cross-sectional aspect ratio effect," J. Wind Eng. Ind. Aerodyn. **213**, 104615 (2021).

Rinoshika, H., Rinoshika, A., and Fujimoto, S., "Passive control on flow structure around a wall-mounted low aspect ratio circular cylinder by using an inclined hole," J. Fluid Sci. Technol. **12**(1), JFST0006 (2017).

Saeedi, M., LePoudre, P. P., and Wang, B.-C., "Direct numerical simulation of turbulent wake behind a surface-mounted square cylinder," J. Fluids Struct. **51**, 20–39 (2014).

Sattari, P., Bourgeois, J. A., and Martinuzzi, R. J., "On the vortex dynamics in the wake of a finite surface-mounted square cylinder," Exp. Fluids **52**(5), 1149–1167 (2012).

Sciacchitano, A., Wieneke, B., and Scarano, F., "PIV uncertainty quantification by image matching," Meas. Sci. Technol. **24**, 045302 (2013).

Sharma, K. R. and Dutta, S., "Flow control over a square cylinder using attached rigid and flexible splitter plate at intermediate flow regime," Phys. Fluids **32**(1), 014104 (2020).

Shao, J. Y., Wen, J. D., and Zhang, L., "Flow control of an elastically mounted square cylinder by using an attached flexible plate," Phys. Fluids **35**(3), 033603 (2023).

Shivashankar, P., and Gopalakrishnan, S., "Review on the use of piezoelectric materials for active vibration, noise, and flow control," Smart Mater. Struct. **29**, 053001 (2020).

Singh, G. and Lakkaraju, R., "Wall-mounted flexible plates in a two-dimensional channel trigger early flow instabilities," Phys. Rev. E **100**(2–1), 023109 (2019).

Sohankar, A., Esfeh, M., Pourjafan, H., Alam, M. M., and Wang, L., "Features of the flow over a finite length square prism on a wall at various incidence angles," Wind Struct. **26**(5), 317–329 (2018), see http://www.techno-press.org/content/?page=article&journal=was&volume=26&num=5&ordernum=6.

Sohankar, A., Khodadadi, M., Rangraz, E., and Alam, M. M., "Control of flow and heat transfer over two inline square cylinders," Phys. Fluids **31**(12), 123604 (2019).

Sumner, D., Rostamy, N., Bergstrom, D. J., and Bugg, J. D., "Influence of aspect ratio on the mean flow field of a surface-mounted finite-height square prism," Int. J. Heat Fluid Flow **65**, 1–20 (2017).

Uffinger, T., Ali, I., and Becker, S., "Experimental and numerical investigations of the flow around three different wall-mounted cylinder geometries of finite length," J. Wind Eng. Ind. Aerodyn. **119**(1), 13–27 (2013).

Wang, H., Peng, S., Li, Y., and He, X., "Control of the aerodynamic forces of a finite-length square cylinder with steady slot suction at its free end," J. Wind Eng. Ind. Aerodyn. **179**, 438–448 (2018).

Wang, H., Zhao, C., Zeng, L., Alam, M. M., and Tang, H., "Control of the flow around a finite square cylinder with a flexible plate attached at the free end," Phys. Fluids **34**(2), 027109 (2022).

Wang, H., Zhao, X., He, X., and Zhou, Y., "Effects of oncoming flow conditions on the aerodynamic forces on a cantilevered square cylinder," J. Fluids Struct. **75**, 140–157 (2017).

Wang, H. F., Zeng, L. W., Alam, M. M., and Guo, W., "Large Eddy Simulation of the flow around a finite-length square cylinder with free-end slot suction," Wind Struct. **30**(5), 533–546 (2020), see http://www.techno-press.org/content/?page=article&journal=was&volume=30&num=5&ordernum=8.

Wang, H. F. and Zhou, Y., "The finite-length square cylinder near wake," J. Fluid Mech. **638**, 453–490 (2009).

Wang, H. F., Zhou, Y., Chan, C. K., and Lam, K. S., "Effect of initial conditions on interaction between a boundary layer and a wall-mounted finite-length-cylinder wake," Phys. Fluids **18**(6), 065106 (2006).

Wu, J., Qiu, Y. L., Shu, C., and Zhao, N., "Flow control of a circular cylinder by using an attached flexible filament," Phys. Fluids **26**(10), 103601 (2014a).

Wu, J., Shu, C., and Zhao, N., "Numerical study of flow control via the interaction between a circular cylinder and a flexible plate," J. Fluids Struct. **49**, 594–613 (2014b).

Xu, M., Wu, M., and Mi, J., "A new type of self-excited flapping jets due to a flexible film at the nozzle exit," Exp. Therm. Fluid Sci. **106**, 226–233 (2019).

Yarusevych, S., Sullivan, P. E., and Kawall, J. G., "Smoke-wire flow visualization in separated flows at relatively high velocities," AIAA J. **47**(6), 1592–1595 (2009).

Zhao, C., Wang, H., Zeng, L., Alam, M. M., and Zhao, X., "Effects of oncoming flow turbulence on the near wake and forces of a 3D square cylinder," J. Wind Eng. Ind. Aerodyn. **214**, 104674 (2021).

Zhang, H. Y., Zhao, Y. K., Tian, X. L., Wang, X. L., and Liu, H., "Symmetry breaking of a closed flexible filament behind a rigid plate at low Reynolds numbers," Phys. Fluids **35**(2), 024110 (2023).

Zheng, C. and Zhang, Y., "Computational Fluid Dynamics study on the performance and mechanism of suction control over a high-rise building," Struct. Des. Tall Spec. Build. **21**(7), 475–491 (2012).

Zhou, Y. and Yiu, M. W., "Flow structure, momentum and heat transport in a two-tandem-cylinder wake," J. Fluid Mech. **548**, 17–48 (2006).